

THE STRUCTURE OF THE PHOTON*

STEFAN SÖLDNER-REMBOLD

Albert-Ludwigs-Universität Freiburg, Hermann-Herder-Str. 3

D-79104 Freiburg, Germany

E-mail: soldner@ruhpb.physik.uni-freiburg.de

The structure of the photon is studied in high energy photon-proton interactions at HERA and photon-photon interactions at LEP. The status of these measurements is reviewed.

1 Introduction

The photon is one of the fundamental gauge bosons of the Standard Model without self-couplings and without intrinsic structure. However, at high energies photon-hadron and photon-photon interactions are dominated by quantum fluctuations of the photons into fermion-antifermion pairs and into vector mesons which have the same spin-parity ($J^{PC} = 1^{--}$) as the photon. This is called photon structure. Electron-positron collisions at LEP and positron-proton collisions at HERA are an ideal laboratory for studying photon structure in the interactions of quasi-real and virtual photons, testing predictions of both Quantum Electrodynamics (QED) and Quantum Chromodynamics (QCD).

2 Electron-photon scattering

If one of the scattered electrons in e^+e^- collisions is detected (tagged), the process $e^+e^- \rightarrow e^+e^- + \text{hadrons}$ (Fig. 1) can be regarded as deep-inelastic scattering of an electron^a on a quasi-real photon which has been radiated by the other electron beam. The cross-section is written as

$$\frac{d^2\sigma_{e\gamma \rightarrow e+\text{hadrons}}}{dx dQ^2} = \frac{2\pi\alpha}{x Q^4} \left[(1 + (1-y)^2) F_2^\gamma(x, Q^2) - y^2 F_L(x, Q^2) \right], \quad (1)$$

where α is the fine structure constant and

$$Q^2 = -q^2 = -(k - k')^2$$

is the negative four-momentum squared of the virtual photon γ^* and

$$x = \frac{Q^2}{2p \cdot q} = \frac{Q^2}{Q^2 + W^2 + P^2}$$

$$y = \frac{p \cdot q}{p \cdot k}$$

*Invited talk given at the XVIII International Symposium on Lepton Photon Interactions, Hamburg, Germany, July 28–August 1, 1997

^aIn this paper positrons are also referred to as electrons

are the usual dimensionless variables of deep-inelastic scattering. $W^2 = (q + p)^2$ is the squared invariant mass of the hadronic final state. The negative four-momentum squared, $P^2 = -p^2$, of the quasi-real target photon is approximately zero and therefore usually neglected. In leading order (LO) the photon structure function $F_2^\gamma(x, Q^2)$ is related to the sum over the quark densities of the photon weighted by the quark charge e_q

$$F_2^\gamma(x, Q^2) = 2x \sum_q e_q^2 f_{q/\gamma}(x, Q^2)$$

with $f_{q/\gamma}(x, Q^2)$ being the probability to find a quark flavour q with the momentum fraction x (sometimes denoted by x_γ) in the photon. For measuring $F_2^\gamma(x, Q^2)$ the values of Q^2 and y can be reconstructed from the energy, E_{tag} , and the angle, θ_{tag} , of the tagged electron and the beam energy E_{beam} via the relations

$$Q^2 \approx 2E_{\text{beam}}E_{\text{tag}}(1 - \cos \theta_{\text{tag}})$$

$$y \approx 1 - \frac{E_{\text{tag}}}{E_{\text{beam}}} \cos^2 \frac{\theta_{\text{tag}}}{2}.$$

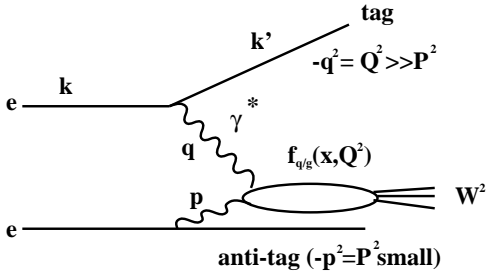


Figure 1: Deep-inelastic $e\gamma$ scattering: $k(k')$ denotes the four-momentum of the incoming (scattered) electron and $q(p)$ the four-momentum of the virtual (quasi-real) photon.

In order to identify an electron in the detector, the tag energy E_{tag} has to be large, i.e. only low values of y are accessible ($y^2 \ll 1$). The contribution of the cross-section term proportional to the longitudinal structure function F_L^γ is therefore negligible.

The reconstruction of x , however, relies heavily on the measurement of the invariant mass W from the energies E_h and momenta \vec{p}_h of the final state hadrons h :

$$W^2 = \left(\sum_h E_h \right)^2 - \left(\sum_h \vec{p}_h \right)^2.$$

Unfolding of the x dependence of the structure function therefore requires that the hadronic final state in $e\gamma$ events is well measured and well simulated by the Monte Carlo models.

2.1 Hadronic energy flows

OPAL¹, ALEPH² and DELPHI³ have studied the hadronic energy flow per event, $1/N \cdot dE/d\eta$, as a function of the pseudorapidity $\eta = -\ln \tan \theta/2$, where the sign of η is chosen in such way that the tag electron is always at negative η . OPAL has measured the energy flow at medium Q^2 ($\langle Q^2 \rangle = 13 \text{ GeV}^2$) and at high Q^2 ($\langle Q^2 \rangle = 135 \text{ GeV}^2$)¹. In Fig. 2 the energy flows are compared to the two QCD based Monte Carlo generators HERWIG⁴ and PYTHIA⁵. The data distributions have been corrected for detector effects. The generator F2GEN is used to model the unphysically extreme case of a two-quark state in the $\gamma^*\gamma$ centre-of-mass system with an angular distribution as in lepton pair production from two real photons (“pointlike”). The “perimiss” sample is a physics motivated mixture of pointlike and peripheral interactions, where peripheral means that the transverse momentum of

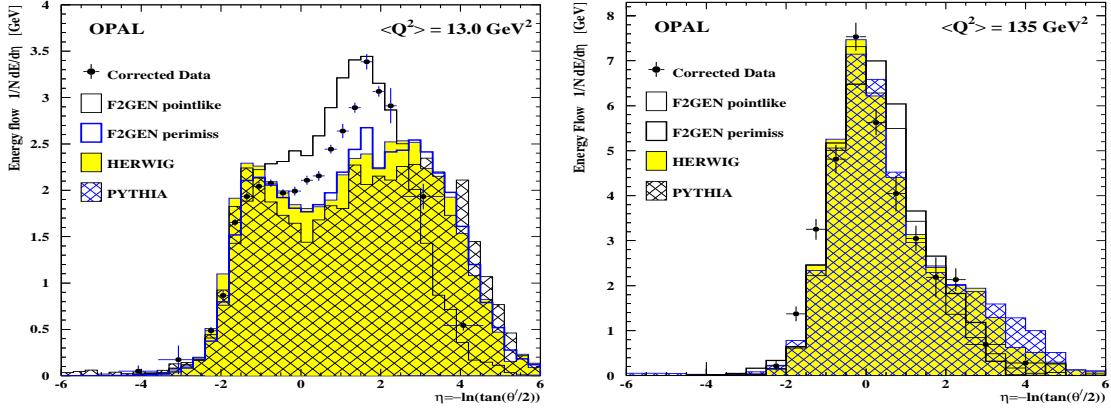


Figure 2: The energy flow per event as a function of the pseudorapidity η in different Q^2 ranges compared to the HERWIG, PYTHIA and F2GEN Monte Carlo models. The data have been corrected for detector effects.

the outgoing quarks is given by an exponential distribution as if all the photons interacted as pre-existing hadrons.

Significant discrepancies exist between the data and all of the Monte Carlo models. The agreement improves at higher Q^2 . Since x and Q^2 are correlated, the discrepancies at low Q^2 are observed also at low x . These discrepancies between the data and the Monte Carlo model for the hadronic final state are the dominant source of systematic uncertainty in the unfolding of $F_2^\gamma(x, Q^2)$ ¹.

Tuning of the Monte Carlo to improve the modelling of the hadronic final state is complicated and must be done with care in order to avoid a bias of the result of the unfolding towards the parametrisation of the parton distribution functions used in the tuned Monte Carlo. ALEPH² has measured the energy flow in tagged event for $\langle Q^2 \rangle = 14.2 \text{ GeV}^2$. The distributions have not been corrected for detector effects. The energy flow shown in Fig. 3 is compared to the HERWIG generator⁴ and a Monte Carlo which consists of a mixture of Quark Parton Model (QPM) and Vector Meson Dominance (VDM) similar to the F2GEN generator. In addition, a modified version of HERWIG (“HERWIG+power law p_T ”) was used. The modification is based on studies of the photon remnant by ZEUS⁶. In standard HERWIG a Gaussian distribution is used to describe the limitation of the transverse momentum of the outgoing partons with respect to the initial target photon. In the modified

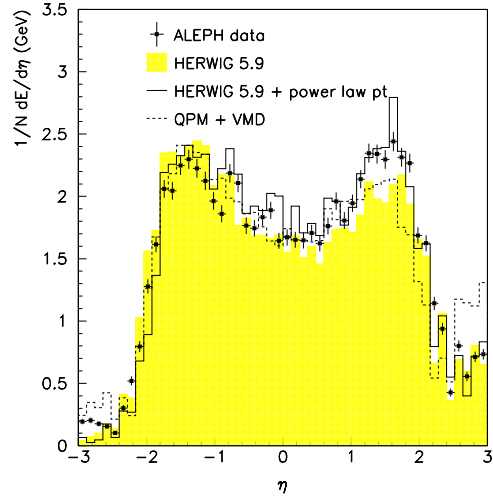


Figure 3: The energy flow per event as a function of η , compared to a QPM+VDM model, the standard and the tuned version of HERWIG.

HERWIG the Gaussian is replaced by a power law spectrum. The agreement with the data improves. A similar study was performed earlier in Ref. 7 using OPAL data. It is expected that such improvements of the Monte Carlo models will significantly reduce the systematic error of the structure function measurements for hadronic events.

2.2 The photon structure function F_2^γ at high Q^2

Even though the concept of the photon structure function F_2^γ has been developed in analogy to the formalism of the nucleon structure functions F_2^N , there are important differences: $F_2^\gamma(x, Q^2)$ increases with Q^2 for all x and this positive scaling violation is expected already within the parton model. Furthermore, F_2^γ is large for high x , whereas F_2^N decreases at large x . These differences are due to the additional perturbative $\gamma \rightarrow q\bar{q}$ splitting which does not exist for the nucleon.

For large x and asymptotically large Q^2 the value of F_2^γ can therefore be calculated from perturbative QCD⁸. The next-to-leading order (NLO) result⁹ can be written as

$$\frac{F_2^\gamma}{\alpha} = \frac{a(x)}{\alpha_s(Q^2)} + b(x), \quad (2)$$

where $a(x)$ and $b(x)$ are calculable functions which diverge for $x \rightarrow 0$ and α_s is the strong coupling constant. The first term corresponds to the LO result by Witten⁸. The measurement of F_2^γ could be a direct measurement of Λ_{QCD} if it were not for the large non-perturbative contributions due to bound states. These contributions are large at all experimentally accessible values of Q^2 .

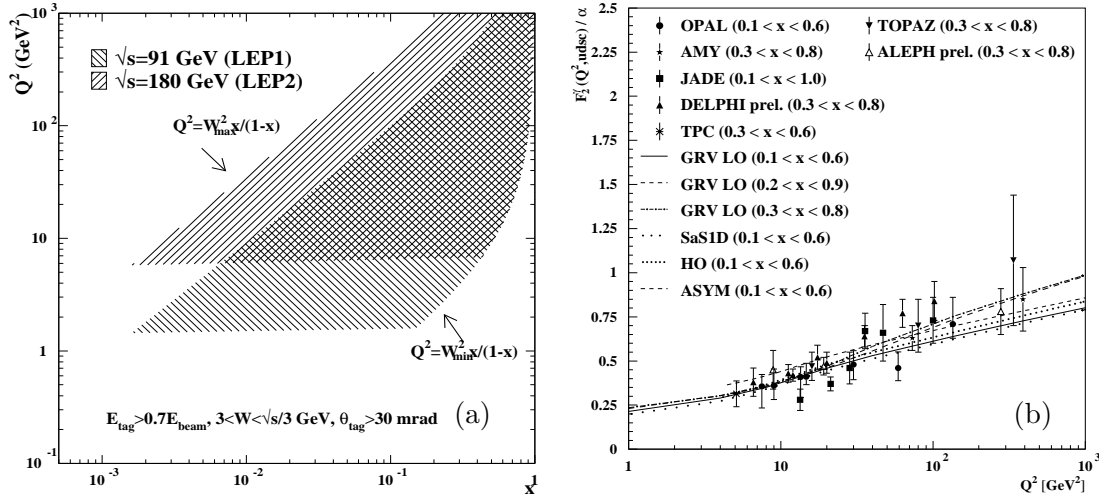


Figure 4: a) Kinematical coverage of the (Q^2, x) plane at LEP1 and LEP2. b) The photon structure function F_2^γ/α as a function of Q^2 .

The photon structure function $F_2^\gamma(x, Q^2)$ can be measured at LEP in the range $x > 10^{-3}$ and $1 < Q^2 < 10^3$ GeV² which makes it possible to study the QCD evolution of F_2^γ in a wide range of x and Q^2 (Fig. 4a).

The evolution of F_2^γ with $\ln Q^2$ is shown in Fig. 4b using the currently available F_2^γ measurements for 4 active flavours. The data are compared to the LO GRV¹⁰ and the SaS-1D¹¹ parametrisations, and to a higher order (HO) prediction based on the NLO GRV parametrisation for light quarks and on the NLO charm contribution calculated in Ref. 12. The data are measured in different x ranges. The comparison of the LO GRV curves for these x ranges shows that for $Q^2 > 100 \text{ GeV}^2$ significant differences are expected. An augmented asymptotic prediction for F_2^γ is also shown. The contribution to F_2^γ from the three light flavours is approximated by Witten's leading order asymptotic form⁸. This has been augmented by adding a charm contribution evaluated from the Bethe-Heitler formula¹³, and an estimate of the hadronic part of F_2^γ , which essentially corresponds to the hadronic part of the LO GRV parametrisation. In the region of medium x values studied here this asymptotic prediction in general lies higher than the GRV and SaS predictions but it is still in agreement with the data. The importance of the hadronic contribution to F_2^γ decreases with increasing x and Q^2 , and it accounts for only 15 % of F_2^γ at $Q^2 = 59 \text{ GeV}^2$ and $x = 0.5$.

As predicted by QCD the evolution of F_2^γ leads to a logarithmic rise with Q^2 , but theoretical and experimental uncertainties are currently too large for a precision test of perturbative QCD.

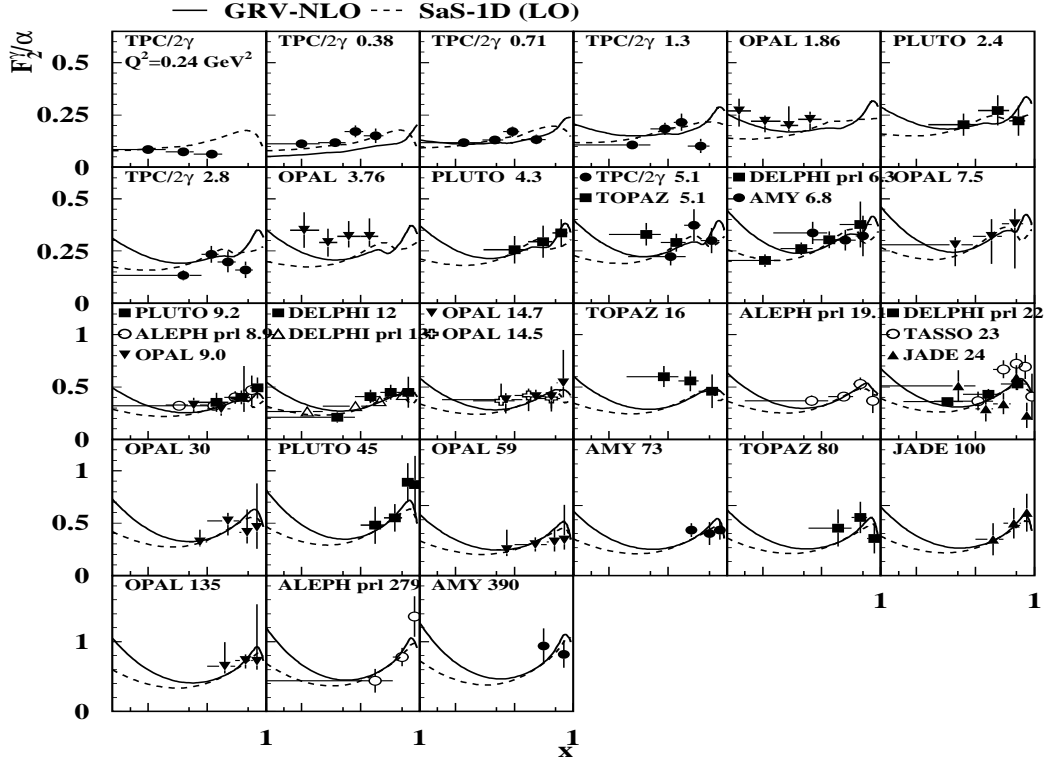


Figure 5: Measurements of the photon structure function F_2^γ in bins of x and Q^2 .

2.3 The photon structure function F_2^γ at low x

All currently available measurements¹⁴ of the photon structure function are shown in Fig. 5. The data are compared to the NLO GRV¹⁰ parametrisation and the LO SaS-1D¹¹ parametrisation. If the photon is purely hadron-like at low x , a rise of the photon structure function is expected in the low x region for not too small Q^2 , similar to the rise of the proton structure function observed at HERA. Only with the high statistics and high energy LEP2 data will it be possible to access regions in x and Q^2 where the rise of F_2^γ could be observed. An interesting new low x measurement of F_2^γ is presented by OPAL in the x and Q^2 ranges $2.5 \times 10^{-3} < x < 0.2$ and $1.1 < Q^2 < 6.6 \text{ GeV}^2$. The measurement is consistent with a possible rise within large systematic errors. It should be noted that the OPAL points are significantly higher than the previous measurement by TPC/ 2γ in a similar kinematic range.

In the kinematic region of the LEP measurements, the effect of the P^2 evolution can become quite important. The ALEPH and OPAL $F_2^\gamma(x, Q^2)$ measurements have all not been corrected for this effect, i.e. they are actually measurements of $F_2^\gamma(x, Q^2, P^2)$. OPAL estimates that the effect of the non-zero virtuality P^2 could increase their low x measurement of F_2^γ by about 10 % for $P^2 = 0$. This estimate is based on the P^2 dependent parametrisation of the parton distributions by Schuler and Sjöstrand¹⁵.

Since there is little experimental information about the low x region, Gurvich, Abramowicz and Levy (GAL) have tried to use the F_2^p data at low x in order to constrain their new F_2^γ parametrisation¹⁶. Gribov factorisation is assumed, based on the idea that at high enough centre-of-mass energies all total hadronic cross-sections are dominated by an universal Pomeron trajectory which allows to relate hadron and photon induced cross-sections. Furthermore this factorisation assumption should also hold for virtual photons at low x . The proton structure function F_2^p and the photon structure function F_2^γ are then related by the total γp and pp cross-sections:

$$F_2^\gamma(x, Q^2) = F_2^p(x, Q^2) \frac{\sigma_{\gamma p}(W^2)}{\sigma_{pp}(W^2)}.$$

The total cross-section are obtained from a Donnachie-Landshoff parametrisation¹⁷ of the data (see Sect. 6). This procedure is used to obtain pseudo-data for F_2^γ at low x . The evolution of the parton densities is done using a LO Altarelli-Parisi evolution with a starting scale $Q_0^2 = 4 \text{ GeV}^2$. The predicted rise is much lower at low x than predicted by the LO GRV parametrisation which is also shown in Fig. 6.

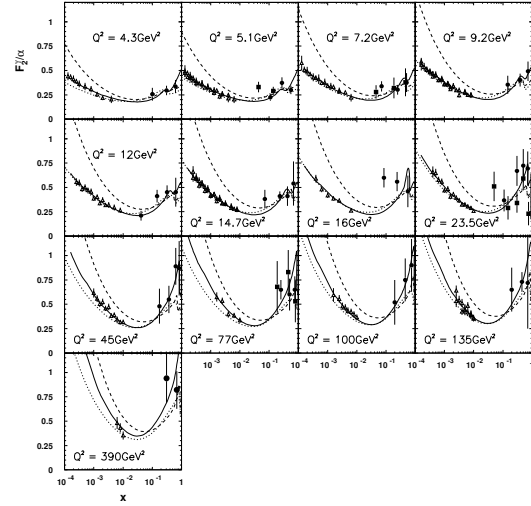


Figure 6: The GAL parametrisation (continuous line) compared to the F_2^γ data and the scaled F_2^p data using Gribov factorisation. The dashed line is the LO GRV parametrisation and the dotted line the SaS parametrisation.

2.4 Azimuthal correlations

Only the structure function F_2^γ has so far been determined directly from measurements of double-differential cross-sections for $e\gamma$ events with hadronic or leptonic final states. It has been pointed out¹⁸ that azimuthal correlations in the final-state particles from two-photon collisions are sensitive to additional structure functions. Azimuthal correlations can thus supplement the direct measurement of structure functions. ALEPH¹⁹, L3²⁰ and OPAL²¹ have measured azimuthal correlations using single-tag $e^+e^- \rightarrow e^+e^-\mu^+\mu^-$ events.

For single-tag events two independent angles can be defined in the $\gamma\gamma^*$ centre-of-mass system assuming that the target photon direction is parallel to the beam axis: The azimuthal angle χ is the angle between the planes defined by the $\gamma\gamma^*$ axis and the two-body final state and the $\gamma\gamma^*$ axis and the tagged electron. The variable $\eta = \cos\theta^*$ is defined by the angle θ^* between the μ^- and the $\gamma\gamma^*$ axis.

Neglecting the longitudinal component of the target photon, the cross-section can be written as ($F_2^\gamma = 2xF_T^\gamma + F_L^\gamma$):

$$\frac{d\sigma(e\gamma \rightarrow e\mu^+\mu^-)}{dx dy d\eta d\chi/2\pi} \approx \frac{2\pi\alpha^2}{Q^2} \left(\frac{1 + (1-y)^2}{xy} \right) \left[2x\tilde{F}_T^\gamma + \tilde{F}_L^\gamma - \tilde{F}_A^\gamma \cos\chi + \frac{\tilde{F}_B^\gamma}{2} \cos 2\chi \right]. \quad (3)$$

The conventional structure functions are recovered by integration over η and χ : $F_i^\gamma = \int_{-1}^1 \int_0^{2\pi} \frac{d\chi d\eta}{2\pi} \tilde{F}_i^\gamma$ ($i = 2, A, B$). The structure functions F_T and F_L are related to the scattering of transverse and longitudinally polarized virtual photons on a transverse target photon, respectively. F_A^γ is related to the interference terms between longitudinal and transverse photons and F_B^γ to the interference term between purely transverse photons. The longitudinal structure function F_L^γ has been shown to be equal to the structure function F_B^γ in leading order and for massless muons, although coming from different helicity states of the photons.

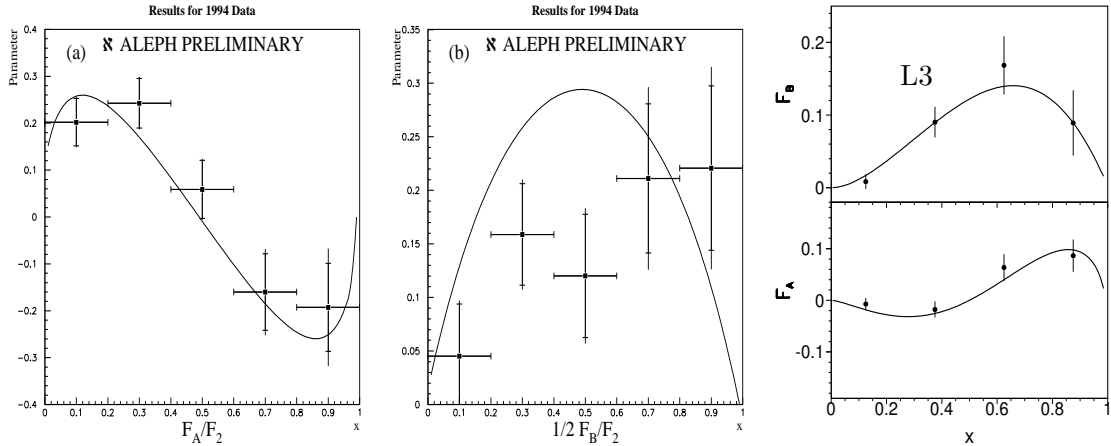


Figure 7: The ratio of structure functions, F_A^γ/F_2^γ and $1/2 \cdot F_B^\gamma/F_2^\gamma$, for the process $e^+e^- \rightarrow e^+e^-\mu^+\mu^-$. The lines show the QED expectation. The ALEPH measurement is not corrected for the cut $|\eta| < 0.8$. The Q^2 ranges are $\langle Q^2 \rangle = 8.8 \text{ GeV}^2$ (ALEPH) and $1.4 < Q^2 < 7.6 \text{ GeV}^2$ (L3).

The variation of F_A^γ and F_B^γ with x is in general consistent with QED (Fig.7 and Ref. 21). The measured values are significantly different from zero. Apart from being an interesting test of QED, these results are especially important as a first step towards measuring the additional structure functions for hadronic events using azimuthal correlations. Such a measurement will be much more difficult due to the problems related to the jet finding in hadronic events.

3 Jet production in $\gamma\gamma$ and γp scattering

If the virtuality Q^2 of the probing photon in ep scattering or the virtualities Q^2 and P^2 of both interacting photons in e^+e^- scattering are approximately zero, the photons can be considered to be quasi-real. HERA can then be used as photon-proton collider with γp centre-of-mass energies in the approximate range $40 < W_{\gamma p} < 300$ GeV and LEP2 as a photon-photon collider with $\gamma\gamma$ centre-of-mass energies in the approximate range $10 < W_{\gamma\gamma} < 120$ GeV. Anti-tagged γp events at HERA and anti-tagged $\gamma\gamma$ events at LEP have a median Q^2 of about 10^{-4} GeV² for $Q^2 < 4$ GeV². The anti-tagging condition is fulfilled if no scattered electron was found in the main calorimeters. Events with $Q^2 < 10^{-2}$ GeV² are tagged using small angle calorimeters.

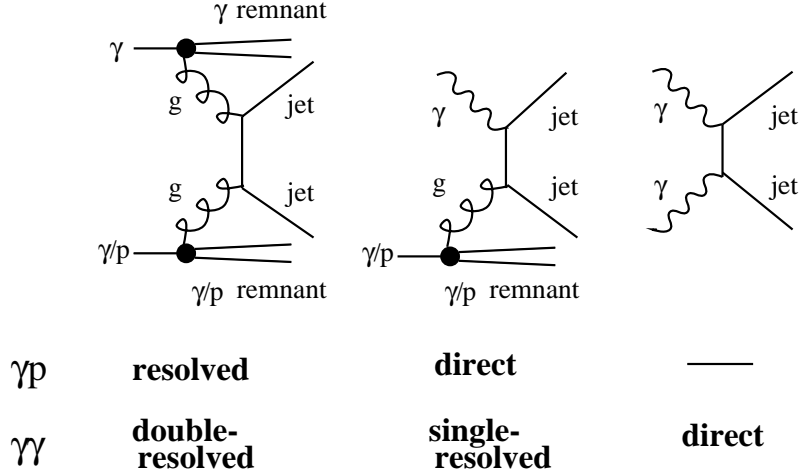
In LO different event classes can be defined in $\gamma\gamma$ and γp interactions. The photons can either interact as bare photons (“direct”) or as hadronic fluctuation (“resolved”). The events are classified by the photon interaction which leads to the nomenclature shown in Fig. 8. In NLO the separation into event classes ceases to be unique, since it depends on the factorisation scale for the photon, and only the sum of the cross-section for the different event classes is well defined.

Within the LO picture we expect two hard jets, i.e. with large transverse energy E_T^{jet} , in the final state in addition to possible photon and/or proton remnants. These jets are related to the underlying parton dynamics and can therefore be used to constrain the structure of the colliding particles, photons and protons. Direct and resolved events can be separated by using the fraction x_γ of the photon’s momentum participating in the hard interaction. The direct events are expected to have $x_\gamma = 1$. For γp events a separation of the event classes has been achieved experimentally by defining the variable²²

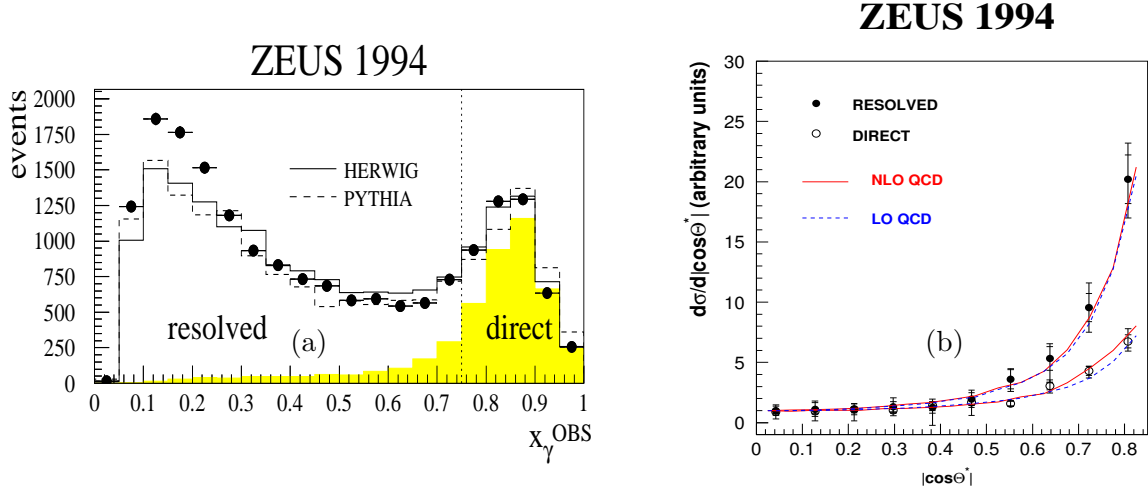
$$x_\gamma^{\text{obs}} = \frac{\sum_{\text{jets}} E_T^{\text{jet}} e^{-\eta^{\text{jet}}}}{2yE_e},$$

with $E_e = 27.5$ GeV being the electron beam energy. The sum runs over the two jets with highest E_T^{jet} and $E_\gamma = yE_e$ is the energy of the initial state photon. For two-jet final states, this observable is equivalent to the LO definition of x_γ . Fig. 9a shows the uncorrected x_γ^{obs} distribution measured by ZEUS in comparison to the LO MC models PYTHIA and HERWIG. The peak at high x_γ^{obs} due to the direct events is observed in the data. However, it is smeared out due to hadronisation, QCD radiation and detector effects.

The measurement of jet cross-sections allows comparisons with perturbative QCD calculations which are based on the matrix elements $M(\cos\theta^*)$ for all possible parton scattering processes. The various matrix elements depend on the parton scattering angle θ^* in the

Figure 8: Examples for leading order processes in $\gamma\gamma$ and γp interactions.

parton-parton centre-of-mass frame. A ZEUS measurement of the different angular distributions is shown in Fig. 9b. The $\cos|\theta^*|$ distribution is here given in the jet-jet centre-of-mass system for resolved ($x_{\gamma}^{\text{obs}} < 0.75$) and direct dijet events ($x_{\gamma}^{\text{obs}} > 0.75$)²³. The dijet invariant mass of these events is larger than 23 GeV. The dominant LO diagrams for direct γp processes involve quark (fermion) exchange whereas those in resolved processes involve gluon (boson) exchange. This leads to different angular distributions which agree well both with the LO QCD curves and with the NLO calculations by Harris and Owens²⁴. Similar results for $\gamma\gamma$ scattering were reported by OPAL²⁵.

Figure 9: a) Uncorrected x_{γ}^{obs} distribution for γp dijet events. b) dijet angular distribution $d\sigma/d|\cos\theta^*|$ in the jet-jet centre-of-mass frame.

As we have seen, jet production is sensitive to the parton content of the photon. In the kinematic range covered by e^+e^- experiments the F_2^{γ} measurements are mainly probing the

quark content of the photon, since the gluon distribution only enters in higher order^b. This is different in $\gamma\gamma$ and γp jet production where a large fraction of the events are due to gluon initiated processes. Measurements of jet production cross-sections can therefore be used to constrain the relatively unknown gluon distribution in the photon.

Different groups have followed different philosophies for extracting information about the parton content of the photon from jet cross-sections. In the first approach hadronic jet cross-sections are measured and compared to calculations which use different parametrisations of the photon's parton densities as input. In the second approach, which is mainly followed by H1, LO parton densities are extracted from the measurements.

For the comparison of theory and experiment it is very important to define suitable jet algorithms. Measurements of jet cross-section in $\gamma\gamma$ and γp interactions are usually made with cone jet finding algorithms²⁸, since resolved photon interactions are similar to hadron-hadron interactions. A problem appears for overlapping jets which can be merged in iterative cone algorithms. This is not described by a NLO calculation which only contains three final state partons²⁹.

Other effects like hadronisation or the underlying event in resolved events are also not contained in the theory. Underlying event is a loose term for additional activity which, for example, can be caused by soft or hard interactions of the photon and proton remnants of the same event. The influence of these effects has to be studied in detail before statements about the parton distributions can be made, since the additional energy in the event directly affects the jet cross-sections. The Monte Carlo models treat this effect by introducing multiple parton interactions (MI).

3.1 Jet shapes

The internal structure of jets was studied by ZEUS³⁰ by measuring jet shapes in photoproduction. The jet shape is defined as the average fraction of E_T^{jet} that lies inside an inner cone of radius r concentric with the jet defining cone:

$$\psi(r) = \frac{1}{N_{\text{jets}}} \sum_{\text{jets}} \frac{E_T(r)}{E_T(r=R)},$$

where $E_T(r)$ is the transverse energy within the inner cone of radius r and N_{jets} the total number of jets. The η^{jet} dependence of the jet shapes is compared at a fixed value for r , $\psi(r=0.5)$, to the PYTHIA prediction with and without multiple interactions (MI) in Fig. 10a. The larger colour charge of gluon jets leads to increased QCD radiation which broadens the jets, an effect which is well known from jet production in e^+e^- scattering. In the forward direction (positive η^{jet}) the fraction of gluon jets in the MC increases, but also the influence of MI increases. Both effects are expected to lead to the broadening of the jets at high η^{jet} which is observed in the data. In Fig. 10b the jet shapes $\psi(r)$ for different E_T^{jet} ranges are also compared to fixed-order perturbative QCD calculations^{29,31}. Jets get narrower with increasing E_T^{jet} . A new parameter R_{sep} was introduced in the calculation to

^bContrary to the proton case, there exists no simple sum rule for the gluon distribution in the photon. A sum rule has been derived by Frankfurt and Gurvich²⁶ and Schuler²⁷.

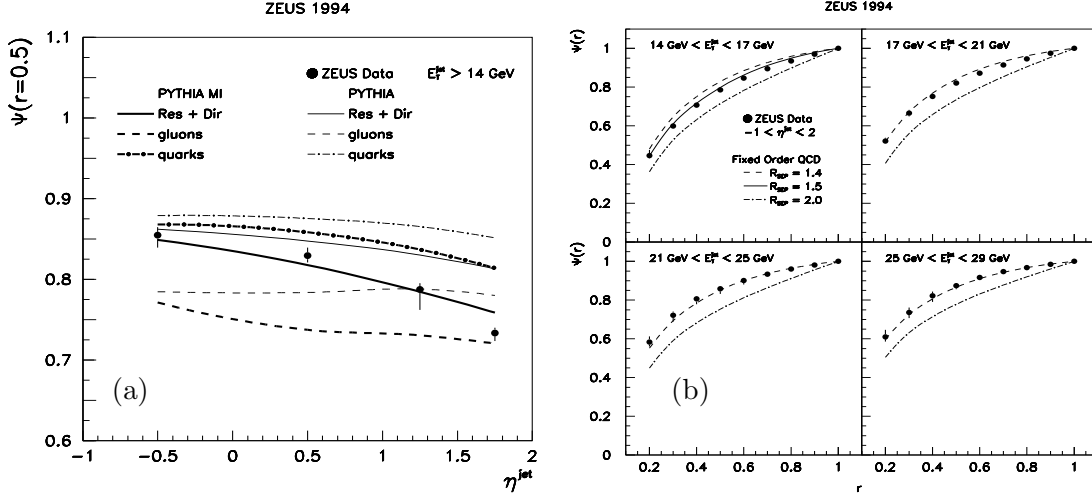


Figure 10: a) Jet shape $\psi(r)$ at a fixed value $r = 0.5$ as a function of η^{jet} for jets with $E_T^{\text{jet}} > 14$ GeV; b) jet shapes $\psi(r)$ as a function of the radius r for jets with $-1 < \eta^{\text{jet}} < 2$ in different E_T^{jet} regions.

mimic the effects of overlapping and merging of jets mentioned in the previous section. Two partons are not merged into a single jet if their separation in the $\eta\phi$ plane is more than R_{sep} . This problem only exists for the iterative cone algorithms used here, whereas the k_T clustering algorithm³² requires no additional parameter R_{sep} . The choice $R_{\text{sep}} = 1.4$ gives a reasonable description of the data, but at low E_T^{jet} a higher R_{sep} is needed. This increase at low E_T^{jet} can be attributed to hadronisation effects and a possible underlying event.

3.2 Inclusive jet cross-sections and NLO calculations

NLO jet cross-sections for $\gamma\gamma$ ^{33,34} and γp interactions^{24,35,36} have been calculated by many authors. To calculate jet cross-sections in perturbative QCD a hard scale is required in the event which is usually the transverse momentum p_T of the final-state partons (or the jet). For the calculation it is assumed that the concept of factorisation can be applied. The LO jet cross-section is written as convolution of the parton density $f_{i/\gamma}$ of the photon and, in the case of γp scattering, the parton density $f_{j/p}$ of the proton with the LO matrix elements M_{ij} for the scattering of two partons i and j :

$$\frac{d\sigma_{\text{ep(ee)}}}{dx_1 dx_2 d\cos\theta^*} \propto \sum_{ij} \frac{f_{i/\gamma}(x_1, p_T^2)}{x_1} \frac{f_{j/p(\gamma)}(x_2, p_T^2)}{x_2} |M_{ij}(\cos\theta^*)|^2.$$

The variables x_1, x_2 are either the momentum fractions x_γ, x_p of the partons in the photon and the proton (for γp scattering) or the momentum fractions x_γ^+, x_γ^- of the partons in the two interaction photons (for $\gamma\gamma$ scattering). In addition the photon flux from the electrons is taken into account using the Weizsäcker-Williams Approximation.

The NLO correction term depends on the two factorisation scales, the renormalisation scale and the cone size R . NLO parton distributions of the photon should be used for

a consistent NLO calculation. Several such NLO parametrisations are available GRV¹⁰, GS96³⁷ and AFG³⁸.

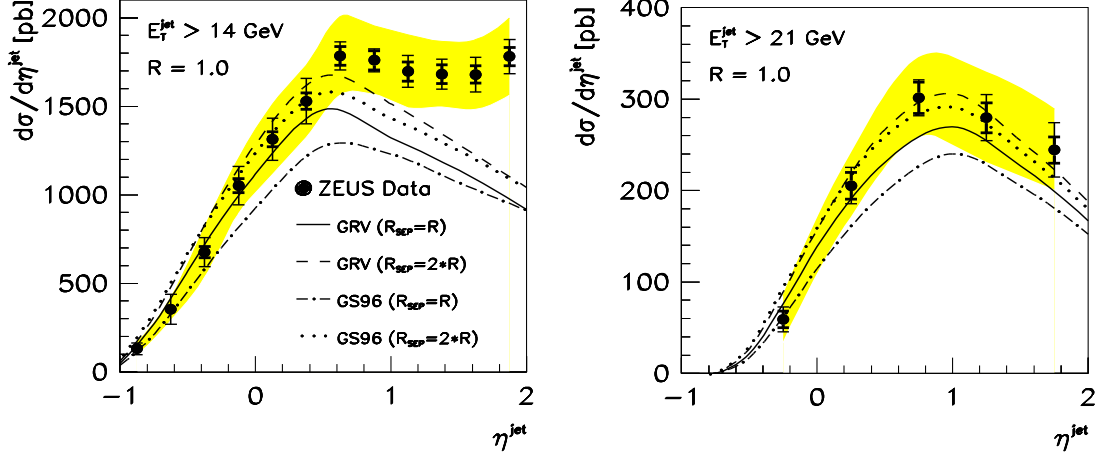


Figure 11: The measured inclusive e^+p jet cross-section as a function of η^{jet} for jets with $E_T^{\text{jet}} > 14$ GeV and $E_T^{\text{jet}} > 21$ GeV using a cone size $R = 1$. The kinematic regime is defined by $Q^2 < 4$ GeV² and $134 < W < 277$ GeV. The bands represent the uncertainty due to the calorimeter energy scale. The curves are the NLO calculations.

ZEUS³⁹ has compared measured inclusive single jet cross-sections in different ranges of E_T^{jet} and η^{jet} to the NLO calculation by Klasen and Kramer³⁶ (Fig. 11). The NLO GRV¹⁰ and the GS96³⁷ parametrizations are used for the photon. The discrepancies are large for smaller E_T^{jet} in the forward region $\eta^{\text{jet}} > 0.5$. This discrepancy disappears at higher E_T^{jet} . The agreement also improves if a smaller cone size is used ($R = 0.7$) which corresponds to an effective increase of the E_T^{jet} threshold compared to $R = 1$. In the region of large discrepancy non-perturbative contributions from the underlying event are expected to be large.

The NLO calculations are given for two values of R_{sep} ($R_{\text{sep}} = R, 2R$) which indicates part of the theoretical uncertainty. The differences between NLO GRV and GS96 are of similar magnitude as the current theoretical and experimental uncertainties. In addition ZEUS has also measured dijet⁴⁰ and multi-jet⁴¹ cross-sections.

Inclusive one-jet and dijet cross-sections have also been measured in $\gamma\gamma$ scattering at an e^+e^- centre-of-mass energy of $\sqrt{s_{ee}} = 58$ GeV at TRISTAN^{42,43} and at $\sqrt{s_{ee}} = 130 - 172$ GeV by OPAL^{44,25}. The E_T^{jet} distribution for dijet events in the range $|\eta^{\text{jet}}| < 2$ measured by OPAL²⁵ at $\sqrt{s_{ee}} = 161 - 172$ GeV is shown in Fig. 12a. The measurements are compared to a NLO calculation of the inclusive dijet cross-section³³ which uses the NLO GRV parametrization for the photon¹⁰. The direct, single- and double-resolved parts and their sum are shown separately. The data points are in good agreement with the calculation except in the first bin where theoretical and experimental uncertainties are large.

To study the sensitivity to the choice of parametrization for the parton distributions of the photon, OPAL has also measured the inclusive dijet cross-section as a function of $|\eta^{\text{jet}}|$ for events with a large double-resolved contribution obtained by requiring $x_\gamma^\pm < 0.8$

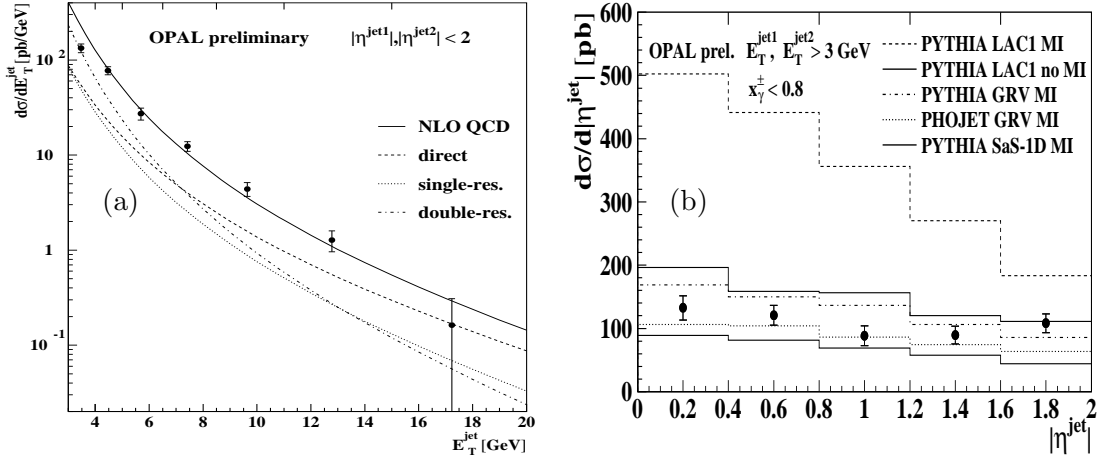


Figure 12: a) The inclusive e^+e^- dijet cross-section as a function of E_T^{jet} for jets with $|\eta^{\text{jet}}| < 2$ using a cone size $R = 1$. b) The inclusive dijet cross-section as a function of $|\eta^{\text{jet}}|$ for jets in mainly double-resolved event with $E_T^{\text{jet}} > 3 \text{ GeV}$ using a cone size $R = 1$.

(Fig. 12b). The variables x_γ^\pm for the two incoming photons are defined in the same way as the γp variable x_γ . Ideally, for direct events without remnant jets $x_\gamma^+ = 1$ and $x_\gamma^- = 1$, whereas for double-resolved events both values x_γ^+ and x_γ^- are expected to be much smaller than 1.

The inclusive dijet cross-section predicted by the two LO QCD models PYTHIA⁵ and PHOJET⁴⁵ differ significantly even if the same photon structure function (here LO GRV) is used. This model dependence reduces the sensitivity to the parametrisation of the photon structure function. Different parametrisations were used as input to the PYTHIA simulation. The LO GRV¹⁰ and SaS-1D parametrisations¹¹ describe the data equally well, but LAC1⁴⁶ which increases the cross-section for gluon-initiated processes overestimates the inclusive dijet cross-section significantly. As in the case of γp scattering a correct treatment of multiple interactions is important. The PYTHIA cross-sections with and without MI using LAC1 differ by more than a factor of two.

3.3 Effective parton densities

Following a procedure developed by Cambridge and Maxwell⁴⁷, H1 has measured the parton distributions of the photon, $f_{i/\gamma}$, using dijet events from γp interactions⁴⁸. This method is based on LO matrix elements. It exploits the fact that in the studied range $0.2 < x_\gamma < 0.7$ the dijet cross-section is dominated by the parton scattering processes $qq' \rightarrow qq'$, $qg \rightarrow qg$ and $gg \rightarrow gg$. The shapes of the angular distributions of the squared matrix elements $|M_{ij}(\cos(\theta^*))|^2$ is similar for all these sub-processes and the rates only differ by the ratio 9/4 of the colour factors. The matrix element can therefore be approximated by a “Single Effective Subprocess” matrix element, M_{SES} , and the parton densities are combined into

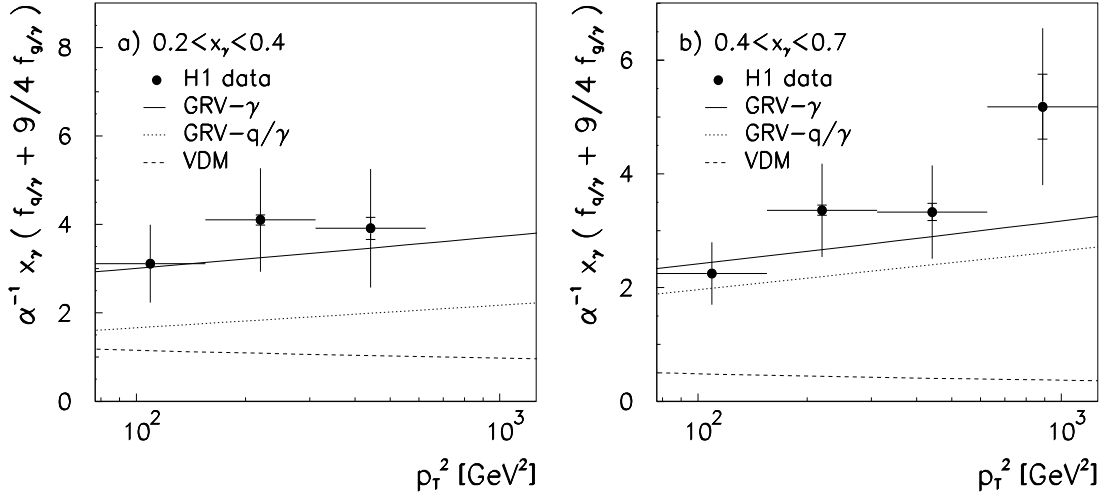


Figure 13: The LO effective parton distribution $\alpha^{-1}x_\gamma\tilde{f}_\gamma(x_\gamma, p_T^2) = \alpha^{-1}x_\gamma(\tilde{f}_{q/\gamma}(x_\gamma, p_T^2) + (9/4)\tilde{f}_{g/\gamma}(x_\gamma, p_T^2))$ as a function of the squared parton transverse momenta, p_T^2 .

effective parton density functions:

$$\tilde{f}_\gamma(x_\gamma, p_T^2) \equiv \sum_{n_f} \left(f_{q/\gamma}(x_\gamma, p_T^2) + f_{\bar{q}/\gamma}(x_\gamma, p_T^2) \right) + \frac{9}{4} f_{g/\gamma}(x_\gamma, p_T^2)$$

$$\tilde{f}_p(x_\gamma, p_T^2) \equiv \sum_{n_f} \left(f_{q/p}(x_\gamma, p_T^2) + f_{\bar{q}/p}(x_\gamma, p_T^2) \right) + \frac{9}{4} f_{g/p}(x_\gamma, p_T^2)$$

where the sum runs over the number of quark flavours, n_f , and p_T is the transverse momentum of the final state parton. The dijet cross-section is then replaced by

$$\frac{d\sigma_{ep}}{dx_\gamma dx_p d\cos\theta^*} \propto \sum_{ij} \frac{\tilde{f}_{i/\gamma}(x_\gamma, p_T^2)}{x_\gamma} \frac{\tilde{f}_{j/p}(x_p, p_T^2)}{x_p} |M_{SES}(\cos\theta^*)|^2.$$

The effective parton distribution \tilde{f}_γ is extracted from the data by measuring the double-differential dijet cross-section $d^2\sigma/dx_\gamma d\log p_T$.

The H1 measurements of the effective parton distributions in two different x_γ ranges ($0.2 < x_\gamma < 0.4$ and $0.4 < x_\gamma < 0.7$) are shown Fig. 13 as a function of p_T^2 . The $\log p_T^2$ dependence of \tilde{f}_γ can now be compared to the QCD evolution using the inhomogeneous DGLAP equations. This is done using the LO GRV parametrisations¹⁰ for the pion and the photon. Assuming that the parton distribution of the pion and the ρ are similar, the purely hadronic (VDM) part of the parton distribution functions is estimated by scaling down the pion distribution with a VDM factor related to the photon- ρ conversion probability. The VDM picture fails to describe the data.

The LO GRV photon parametrisation is constructed to be purely hadronic at very low scales. Due to the pointlike $\gamma \rightarrow q\bar{q}$ term in the DGLAP evolution used to evolve the photon distributions to large scales, one obtains the logarithmic rise observed for the photon

structure function $F_2^\gamma(x, Q^2)$ in $e\gamma$ scattering (see Sect. 2.2 and Fig. 4b). H1 compares the LO GRV distribution of the photon for all partons and for quarks only to their data and both the rise and the normalisation of the data are well reproduced. At lower x_γ the gluon distribution contributes about half, whereas in the range $0.4 < x_\gamma < 0.7$ the quark distribution dominates as expected.

3.4 Leading order gluon densities

The gluon density in the photon has been extracted directly from data by H1 using a two-step procedure. First the distribution of the momentum fraction x_γ is unfolded from the data. In the second step the x_γ distribution of the gluon initiated processes is obtained by applying correction factors which are based on the process definitions used in the Monte Carlo. Since these process definitions are valid in LO, only LO gluon densities can be extracted.

H1 has originally performed this measurement using dijet events⁵⁰. This analysis suffers from two large systematic uncertainties related to the jet finding: the knowledge of the energy scale of the H1 calorimeter and the effect of multiple interactions. In a new analysis of the gluon density, H1 has avoided these uncertainties by using events with high transverse momentum hadrons instead of dijet events⁴⁹.

The price to be paid is a stronger sensitivity to hadronisation effects. Events are required to contain at least one charged particle with transverse momentum $p_T > 2.6$ GeV/c and pseudorapidity $|\eta| < 1$. The variable x_γ^{rec} is reconstructed by summing over all hadrons with $p_T > 2.0$ GeV/c and $|\eta| < 1$:

$$x_\gamma^{\text{rec}} = \frac{1}{E_\gamma} \sum_n p_{Tn} e^{-\eta_n}$$

with E_γ being the photon energy reconstructed from the low Q^2 tagged electron ($Q^2 < 10^{-2}$ GeV²).

After unfolding the LO gluon distribution $x_\gamma g(x_\gamma)/\alpha$ is shown in Fig. 14. Both analyses yield consistent results. The gluon distribution rises at low x_γ , but not as steeply as predicted by the LAC1 distribution⁴⁶. The average scale is given by the average squared transverse momentum of the final state partons. It is 75 (GeV/c)² for the dijet analysis and 38 (GeV/c)² for the hadron analysis.

3.5 Virtual photon structure

The measurement of the photon structure function of virtual photons in e^+e^- collisions requires the detection of both scattered electrons. Only PLUTO⁵¹ has published such a

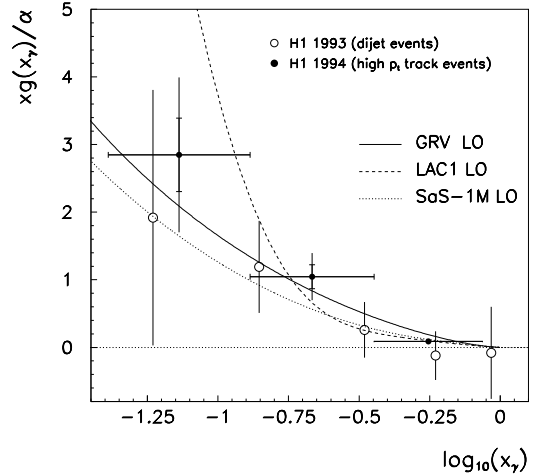


Figure 14: LO gluon distribution $x_\gamma g(x_\gamma)/\alpha$ of the photon.

measurement for a virtuality Q^2 of the probing photon of 5 GeV^2 and a virtuality P^2 of the target photon of 0.35 GeV^2 . More double-tag measurements are to be expected soon from the LEP2 data.

H1 has studied the structure of the virtual photon by measuring the Q^2 dependence of jet production⁵². This introduces a new scale in addition to the transverse energy of the jet which is the relevant scale for real photoproduction ($Q^2 = 0$). In the kinematic range $Q^2 \gg (E_T^*)^2$ the “classical” picture of deep-inelastic scattering (DIS) can be applied where the pointlike virtual photon probes the parton content of the proton (Fig. 15a). The jet transverse energy E_T^* is here calculated in the γ^*p centre-of-mass system. However, a small fraction of the events contains jets with $(E_T^*)^2 > Q^2$. In this case the process can be viewed as probing the structure of the virtual photon using the partonic structure of the proton.

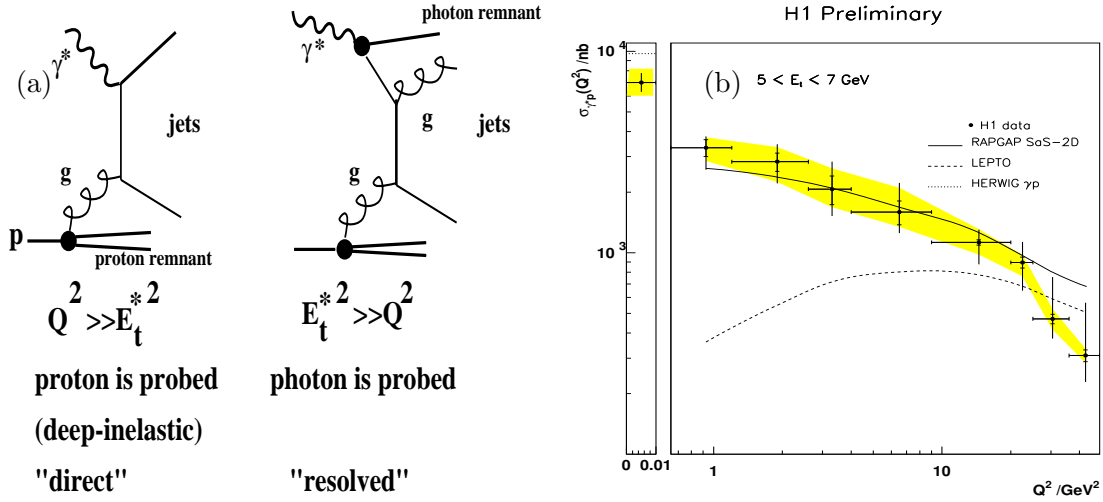


Figure 15: a) Schematic drawing of the two kinematic regimes studied in this analysis. b) Inclusive γ^*p jet cross-section as a function of Q^2 for jets with $5 < E_T^* < 7 \text{ GeV}$ and $-2.5 < \eta^* < -0.5$ (in the γ^*p frame).

H1 has measured the inclusive jet cross-section σ_{γ^*p} for the process $\gamma^*p \rightarrow \text{jet} + X$ as a function of Q^2 for different E_T^* ranges. In Fig. 15b the cross-section $\sigma_{\gamma^*p}(Q^2)$ is shown for jets with $5 < E_T^* < 7 \text{ GeV}$ in comparison to various MC models. LEPTO just simulates deep-inelastic scattering, i.e. it contains no resolved photon processes. RAPGAP contains both deep-inelastic scattering and resolved processes. Within RAPGAP the SaS-2D parton distributions for the photon is used which include a model for the Q^2 suppression for both the non-perturbative VDM and the perturbative anomalous part of the virtual photon.

The DIS picture completely fails to describe the data for scales $Q^2 \ll (E_T^*)^2$, but it approaches the data for $Q^2 \approx (E_T^*)^2 \approx 36 \text{ GeV}^2$. The RAPGAP model with SaS-2D parton distributions is in good agreement with the data over the whole Q^2 range. This observation is complemented by a measurement of the fraction of the photon's energy which is assigned to the photon remnant. This fraction decreases with increasing Q^2 as expected if the resolved photon component is suppressed with increasing Q^2 .

4 Prompt photon production

Prompt photon production in γp interactions at HERA is dominated by the LO direct Compton process $\gamma q \rightarrow \gamma q$ and the resolved processes $qg \rightarrow q\gamma$ and $q\bar{q} \rightarrow g\gamma$. “Prompt” means that these photons are not produced in the fragmentation process or by particle decays. The resolved process could be used to constrain the quark content of the photon at medium x_γ , complementing the F_2^γ measurements from $e\gamma$ scattering. The advantage of having a clean final state without hadronisation uncertainties is however largely compensated by the small cross-section.

ZEUS⁵³ has measured the production cross-section for isolated photons with a transverse energy of $5 \leq E_T^\gamma < 10$ GeV and in the pseudorapidity range $-0.7 \leq \eta^\gamma \leq 0.8$, in association with a jet of $E_T^{\text{jet}} > 5$ GeV in the range $-1.5 \leq \eta^{\text{jet}} \leq 1.8$. Within a total error of more than 25 % the cross-section was found to be in good agreement with NLO calculations by Gordon⁵⁴ using the GS and NLO GRV parton densities for the photon. ZEUS has measured x_γ by summing over the energies E and longitudinal momentum components p_z of the photon and the calorimeter cells which are part of the jet

$$x_\gamma^{\text{meas}} = \frac{\sum_{\gamma, \text{jet}} (E - p_z)}{2y_{\text{JB}}E_e}.$$

The variable $y_{\text{JB}} = \sum_h (E - p_z)/2E_e$ is calculated using the calorimeter cells associated to the final-state hadrons. The x_γ^{meas} distribution of the ZEUS prompt photon signal is shown in Fig. 16. A clear peak at $x_\gamma^{\text{meas}} > 0.8$ is observed. Using the LO Monte Carlo generator PYTHIA about 75 % of the events in this region can be attributed to direct Compton processes with $x_\gamma = 1$ with the remaining 12 % due to resolved events and 13 % due to radiative events where one of the outgoing quarks in a dijet event radiates a photon. More data are needed to obtain a more quantitative constraint for the quark distribution in the photon.

5 $D^{*\pm}$ production in $\gamma\gamma$ and γp interactions

In a similar manner to jet production, open charm production in $\gamma\gamma$ and γp collisions can also be used to constrain the parton content of the photon. The charm production cross-sections have been calculated in NLO for $\gamma\gamma$ ^{55,56} and γp interactions^{57,58,59}. The NLO calculations are either done in the so-called massive^{55,57} or in the so-called massless^{56,58,59} scheme.

In the massive scheme the mass m_c of the charm quark sets the scale for the perturbative QCD calculation. The cross-section is factorized into the matrix elements for the

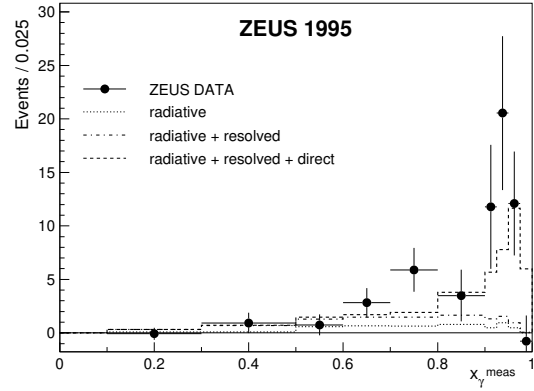


Figure 16: x_γ^{meas} distribution of prompt photons measured by ZEUS.

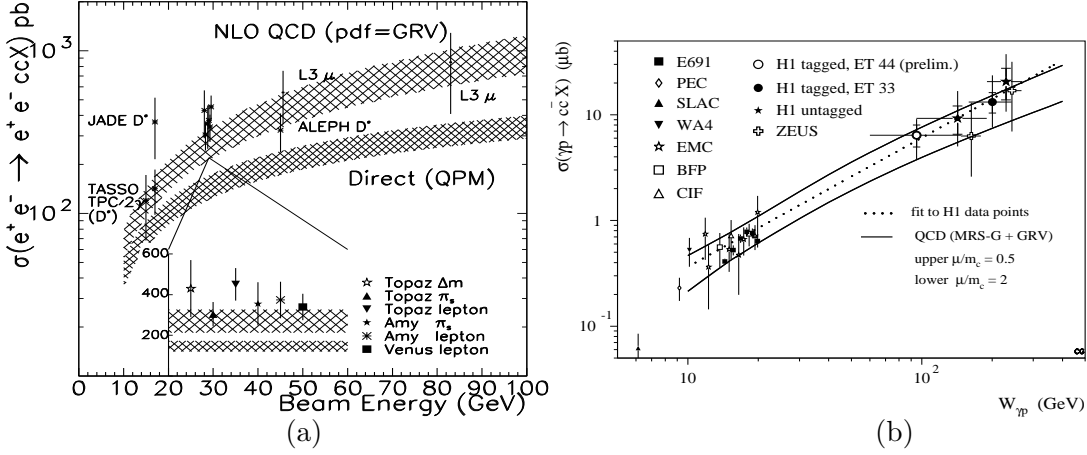


Figure 17: a) Cross-section for the process $e^+e^- \rightarrow e^+e^- c\bar{c}X$ as a function of the electron beam energy; b) cross-section for the process $\gamma p \rightarrow c\bar{c}X$ as a function of the γp centre-of-mass energy $W_{\gamma p}$.

production of heavy quarks and the parton densities for light quarks (q) and gluons. This ‘massive’ approach is expected to be valid if the transverse momenta p_T of the charm quarks are of the same order, $p_T \approx m_c$. At LEP energies only the direct process $\gamma\gamma \rightarrow c\bar{c}$ and the single-resolved process $gq \rightarrow c\bar{c}$ are important. The relevant processes at HERA are $gq \rightarrow c\bar{c}$ and $gg \rightarrow c\bar{c}$. The number of gluon initiated processes depends very much on the parametrisations of the parton densities used. Again, only the sum of the event classes called resolved and direct is well defined in NLO. In the ‘massless’ scheme charm is considered as one of the active flavours in the parton distributions like u, d, s . This scheme is expected to be valid for $p_T \gg m_c$.

The cleanest method to tag open charm is the reconstruction of $D^{*+} \rightarrow D^0\pi^+$ decays. Due to the small branching ratios of the D^0 into charged pions and kaons, this method is statistics limited. ALEPH has measured the charm cross-section $\sigma(e^+e^- \rightarrow e^+e^- c\bar{c}X)$ using 33 ± 8 $D^{*\pm}$ mesons reconstructed in their LEP1 data⁶⁰ with $P_T^{D^*} > 2$ GeV. L3 has measured the charm cross-section in $\gamma\gamma$ interactions at LEP1 and LEP2 by tagging muons from semi-leptonic charm decays in the momentum range $2 < p_\mu < 7$ GeV/ c at LEP1 and $2 < p_\mu < 15$ GeV/ c at LEP2⁶¹. The efficiency to tag muons is less than 10^{-3} leading to large systematic and statistical uncertainties.

The cross-section for the process $e^+e^- \rightarrow e^+e^- c\bar{c}$ as a function of the beam energy is shown in Fig. 17a. The experimental results for various charm tagging methods used by pre-LEP experiments have been extrapolated to obtain

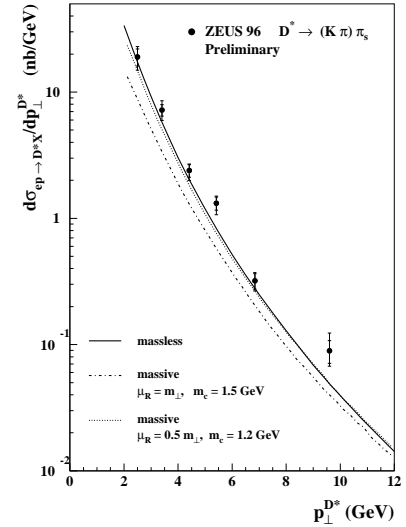


Figure 18: Differential cross-section $d\sigma/dp_T^{D^*}$ in the kinematic region $Q^2 < 4$ GeV², $115 < W < 280$ GeV and $-1.5 < \eta^{D^*} < 1.0$

a total charm cross-section⁶². The upper band shows the full NLO charm cross-section calculated in the massive scheme by Drees et al⁵⁵ and the lower band the contribution from the Born term direct process (Quark Parton Model, QPM). The upper edge of the band is obtained by setting $m_c = 1.3$ GeV with a scale $\mu = m_c$ and the lower edge by setting $m_c = 1.7$ GeV with $\mu = \sqrt{2}m_c$. The data points obtained from the TRISTAN and JADE measurements cluster around the higher edge of the massive NLO calculation which uses the GRV parametrisation.

H1⁶³ and ZEUS^{64,65} have measured $D^{*\pm}$ production cross-sections in γp interactions. Both experiments have derived a cross-section for the process $\gamma p \rightarrow c\bar{c}X$ as a function of the γp centre-of-mass energy $W_{\gamma p}$ ^{63,65}. In Fig. 17b this cross-section is compared to the results of lower energy experiments and to a massive NLO calculation⁵⁷ using the NLO GRV parametrisation. Within the large errors the massive NLO calculations using the GRV parton distributions are in good agreement with the total charm production cross sections measured at LEP and HERA. The cross-section depends very much on the gluon distribution in the photon, e.g. the LAC1 parametrisation gives a much larger cross-section.

The extrapolation of the $D^{*\pm}$ production cross-section to a total $c\bar{c}$ cross-section has large theoretical and experimental uncertainties. These are avoided if differential distributions are measured. ZEUS⁶⁴ has measured the $p_T^{D^*}$ distribution (Fig. 18) and compared it to a massive NLO calculation⁵⁷ using the GRV parametrisation for the photon and to a massless calculation⁵⁸. The normalisation of the massless calculation which uses similar parameters as in the case of the massive calculation with a charm mass $m_c = 1.5$ GeV is in better agreement with the data.

6 Total cross sections

The total cross-sections σ for hadron-hadron and γp collisions are well described by a Regge parametrisation of the form $\sigma = Xs^\epsilon + Ys^{-\eta}$, where \sqrt{s} is the centre-of-mass energy of the hadron-hadron or γp interaction. The first term in the equation is due to Pomeron exchange and the second term is due to Reggeon exchange⁶⁶. Assuming factorisation of the Pomeron term X , the total hadronic $\gamma\gamma$ cross-section $\sigma_{\gamma\gamma}$ can be related to the pp (or $\bar{p}p$) and γp total cross-sections at high centre-of-mass energies $W = \sqrt{s_{\gamma\gamma}}$ where the Pomeron trajectory should dominate:

$$\sigma_{\gamma\gamma} = \frac{\sigma_{\gamma p}^2}{\sigma_{pp}}. \quad (4)$$

A slow rise of the total cross-sections with energy is predicted, corresponding to $\epsilon \approx 0.08$. This rise can also be attributed to an increasing cross-section for parton interactions leading to mini-jets in the final state⁶⁷.

Before LEP $\sigma_{\gamma\gamma}(W)$ has been measured by PLUTO⁶⁸, TPC/2 γ ⁶⁹ and MD1⁷⁰. These experiments have measured at $\gamma\gamma$ centre-of-mass energies W below 10 GeV before the onset of the high energy rise of the total cross-section. Using LEP data taken at $\sqrt{s_{ee}} = 130 - 161$ GeV L3⁷¹ has demonstrated that $\sigma_{\gamma\gamma}(W)$ is consistent with the universal Regge behaviour of total cross-sections in the range $5 \leq W \leq 75$ GeV which was also observed in γp scattering at HERA. The L3 measurement is shown in Fig. 19a together with an OPAL

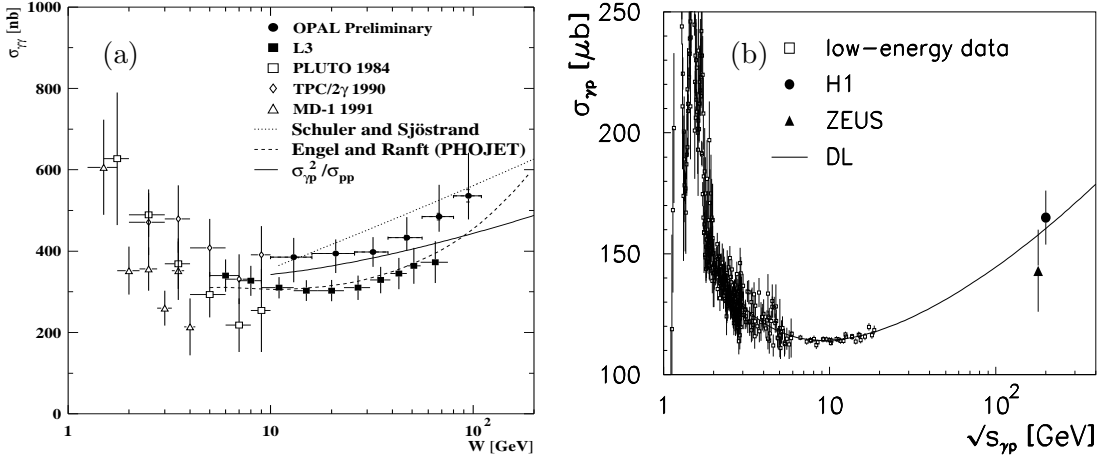


Figure 19: Total cross-section of the process (a) $\gamma\gamma \rightarrow \text{hadrons}$ as a function of $W = W_{\gamma\gamma} = \sqrt{s_{\gamma\gamma}}$ and of the process (b) $\gamma p \rightarrow \text{hadrons}$ as a function of $W_{\gamma p} = \sqrt{s_{\gamma p}}$.

measurement⁷² in the range $10 < W < 110$ GeV using data taken at $\sqrt{s_{ee}} = 161 - 172$ GeV. The observed energy dependence of the cross-section is similar, but the values for $\sigma_{\gamma\gamma}$ are about 20 % higher. The errors are strongly correlated between the W bins in both experiments. Furthermore, L3 has used the Monte Carlo generator PHOJET⁴⁵ for the unfolding, whereas OPAL has averaged the unfolding results of PHOJET and PYTHIA. The unfolded cross-section using PHOJET is about 5 % lower than the central value. In both experiments the cross-sections obtained using PHOJET are lower than the cross-section obtained with PYTHIA. The origin of the remaining discrepancy is not yet understood.

Based on the Donnachie-Landshoff (DL) model¹⁷, the assumption of a universal high energy behaviour of $\gamma\gamma$, γp and pp cross-sections is tested. The parameters X and Y are fitted to the total $\gamma\gamma$, γp and pp cross-sections in order to predict $\sigma_{\gamma\gamma}$ via Eq. 4. This is done assuming that the cross-sections can be related at $\sqrt{s_{\gamma\gamma}} = \sqrt{s_{\gamma p}} = \sqrt{s_{pp}}$. The process dependent fit values for X and Y are taken from Ref. 73 together with the values of the universal parameters $\epsilon = 0.0790 \pm 0.0011$ and $\eta = 0.4678 \pm 0.0059$. This simple ansatz gives a reasonable description of the total $\gamma\gamma$ cross-section $\sigma_{\gamma\gamma}$. Schuler and Sjöstrand⁷⁴ give a total cross-section for the sum of all possible event classes in their model of $\gamma\gamma$ scattering where the photon has a direct, an anomalous and a VDM component. They consider the spread between this prediction and the simple factorisation ansatz as conservative estimate of the theoretical band of uncertainty. The prediction of Engel and Ranft⁴⁵ is also plotted which is implemented in PHOJET. It is in good agreement with the L3 measurement and significantly lower than the OPAL measurement. The steeper rise predicted by Engel and Ranft is in agreement with both measurements.

7 Photon fragmentation function

Closely related to the parton distributions of the photon are the fragmentation functions $D_{q,g}^\gamma(z, M^2)$ of quarks and gluons into photons with z being the fractional momentum

carried by the photon. The photon fragmentation functions $D_{q,g}^\gamma(z, M^2)$ are measured in e^+e^- annihilation at LEP. The time-like scale M^2 is therefore given by the e^+e^- centre-of-mass energy.

As in the case of the photon structure function, the photon fragmentation function is fully calculable in perturbative QCD for asymptotically large M^2 due to the pointlike coupling of the photon to $q\bar{q}$ pairs. At experimentally accessible values of M^2 the non-perturbative contributions are still large and have to be taken into account. Bourhis et al.⁷⁵ have calculated new fragmentation functions with a full treatment of the Beyond Leading Logarithm (BLL) corrections to the perturbative part and with a VDM input for the non-perturbative part.

A first measurement of the quark-to-photon fragmentation function has been published by ALEPH using isolated photons as well as photons which were reconstructed inside hadronic jets⁷⁶. It was pointed out by the authors of Ref. 75 that these measurements cannot be compared directly to the fully inclusive calculations of the photon fragmentation functions due to phase space restrictions imposed by the jet algorithm used. OPAL⁷⁷ has therefore measured the fully inclusive energy spectrum for photons with energy $E_\gamma > 10$ GeV in hadronic Z^0 decays. The huge background from photons due to hadron decays (e.g. $\pi^0 \rightarrow \gamma\gamma$) is subtracted using a fitting method. The data shown in Fig. 20 are in agreement with the models by Bourhis et al.⁷⁵, Duke and Owens⁷⁸ and by Glück et al.⁷⁹. The differences between the GRV LO calculation and the higher order (HO) calculation with and without the non-perturbative corrections (HO_{PL}) is much smaller than the experimental errors.

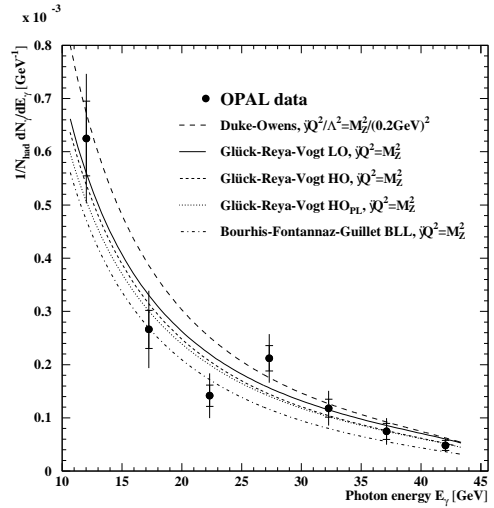


Figure 20: Distribution of the photon energy E_γ in hadronic Z^0 decays.

8 Conclusions

Interactions of photons via quantum fluctuations can be described using a structure functions formalism. The hadronic structure function $F_2^\gamma(x, Q^2)$ of the photon is measured in $e\gamma$ scattering at LEP in the range $x > 10^{-3}$ and $1 < Q^2 < 10^3$ GeV². The logarithmic rise of F_2^γ with Q^2 for medium x and large Q^2 is observed as predicted by perturbative QCD. At low x LEP will be able to study the region where the onset of the rise of F_2^γ is expected from the HERA data on the proton structure function.

The parton content of the photon is also measured in $\gamma\gamma$ and γp interactions at LEP and HERA. Jet production and high p_T hadron production are especially sensitive to the gluon distribution in the photon.

The GRV, SaS, GS and LAC parton distributions of the photons are currently the most widely used parametrisations. Parametrisations with a large gluon distribution like

LAC1 are disfavoured by the data. The other distributions are consistent with most of the available measurements.

H1 has presented new results on the structure of virtual photons from the Q^2 dependence of jet production. More information about the interactions of photons at low and medium Q^2 are to be expected in the near future from the measurement of double-tagged $\gamma^*\gamma^*$ events at LEP.

First measurements by L3 and OPAL of the energy dependence of the total $\gamma\gamma$ cross-section for hadron production show the rise characteristic of hadronic interactions.

Acknowledgements

I want to thank the HERA and the LEP collaborations for providing all the interesting results. My apologies to the CLEO and to the L3 collaboration for not covering their results on form factors and glueball searches. I am also very grateful to Jon Butterworth, John Dainton, Albert De Roeck, Martin Erdmann, Alex Finch, Maria Kienzle, Michael Klasen, Aharon Levy and Richard Nisius for their support and advice.

References

1. OPAL Coll., K. Ackerstaff et al., *Z. Phys.* **C74** (1997) 33; paper LP-159 submitted to this conference.
2. ALEPH Coll., paper LP-253 submitted to this conference.
3. DELPHI Coll., paper 416 submitted to EPS'97, Jerusalem, August 1997.
4. G. Marchesini et al., *Comp. Phys. Comm.* **67** (1992) 465.
5. T. Sjöstrand, *Comp. Phys. Commun.* **82** (1994) 74 and LU-TP-95-20 (1995).
6. ZEUS Coll., M. Derrick et al., *Phys. Lett.* **B354** (1995) 163.
7. J. Lauber et al., *proceedings of PHOTON '97*, Egmond aan Zee, NL (1997).
8. E. Witten, *Nucl. Phys.* **B120** (1977) 189.
9. W.A. Bardeen, A.J. Buras, *Phys. Rev.* **D20** (1979) 166; *Phys. Rev.* **D21** (1980) 2041.
10. M. Glück et al., *Phys. Rev.* **D46** (1992) 1973; *Phys. Rev.* **D45** (1992) 3986.
11. G. A. Schuler, T. Sjöstrand, *Z. Phys.* **C68** (1995) 607.
12. E. Laenen et al, *Phys. Rev.* **D49** (1994) 5753.
13. E. Witten, *Nucl. Phys.* **B104** (1976) 445.
14. A compilation can be found in D. Morgan et al, *J. Phys. G, Nucl. Part. Phys.* **20** (1994) A1; PLUTO Coll., Ch. Berger et al., *Phys. Lett.* **B142** (1984) 111; *Nucl. Phys.* **B281** (1984) 365; JADE Coll., W. Bartel et al., *Z. Phys.* **C24** (1984) 231; TASSO Coll., M. Althoff et al., *Z. Phys.* **C31** (1986) 527; TPC/2 γ Coll., H. Aihara et al., *Phys. Rev. Lett.* **58** (1987) 97; *Z. Phys.* **C34** (1987) 1; TOPAZ Coll., K. Muramatsu et al., *Phys. Lett.* **B332** (1994) 477; AMY Coll., S.K. Sahu et al., *Phys. Lett.* **B346** (1995) 208 ($Q^2 = 73, 390 \text{ GeV}^2$); DELPHI Coll., P. Abreu et al., *Z. Phys.* **C69** (1996) 223 ($Q^2 = 12 \text{ GeV}^2$); AMY Coll., T. Kojima et al., *Phys. Lett.* **B400** (1997) 395; ($Q^2 = 6.8 \text{ GeV}^2$); OPAL Coll., K. Ackerstaff et al, *Z. Phys.* **C74** (1997) 33 ($Q^2 = 7.5, 14.7, 135 \text{ GeV}^2$); CERN-PPE/97-87 ($Q^2 = 9, 14.5, 30, 59 \text{ GeV}^2$); CERN-

- PPE/97-103 ($Q^2 = 1.86, 3.76 \text{ GeV}^2$); ALEPH Coll., paper LP-315 submitted to this conference. DELPHI Coll., paper 416 submitted to EPS'97, Jerusalem, August 1997, and private communication ($Q^2 = 6.3, 13, 22 \text{ GeV}^2$).
15. G. Schuler, T. Sjöstrand, *Phys. Lett.* **B376** (1996) 193.
 16. H. Abramowicz, E. Gurvich, A. Levy, paper LP-235 submitted to this conference.
 17. A. Donnachie, P. V. Landshoff, *Phys. Lett.* **B296** (1992) 227.
 18. C. Peterson et al., *Nucl. Phys.* **B229** (1983) 301; CELLO Coll., H.-J. Behrend et al., *Z. f. Phys.* **C43** (1989) 1; J. H. Field, *proc. of Photon '95*, Sheffield, U.K., eds. D. J. Miller, S. L. Cartwright, V. Khoze, World Scientific, Singapore, 490 (1995); N. Arteaga et al., *proc. of Photon '95*, Sheffield, U.K.; *Phys. Rev.* **D52** (1995) 4920; *Phys. Rev.* **D53** (1996) 2854; P. Aurenche et al., in *Physics at LEP2*, CERN 96-01, p.301 (1996).
 19. C. Brew et al., *proc. of PHOTON '97*, Egmond aan Zee, NL (1997).
 20. L3 Coll., paper submitted to EPS'97, Jerusalem, August 1997.
 21. OPAL Coll., K. Ackerstaff et al, *Z. Phys.* **C74** (1997) 49.
 22. ZEUS Coll., M. Derrick et al., *Phys. Lett.* **B348** (1995) 665.
 23. ZEUS Coll., M. Derrick et al., *Phys. Lett.* **B384** (1996) 401.
 24. B.W. Harris, J.F. Owens, *Phys. Rev.* **D56** (1997) 4007.
 25. OPAL Coll., paper LP-201 submitted to Lepton-Photon 1997.
 26. L.L Frankfurt, E.G. Gurvich, hep-ph/9505406.
 27. G.A. Schuler, CERN-TH/95-153 (hep-ph/9506279).
 28. CDF Coll., F. Abe et al, *Phys. Rev.* *D45* (1992) 1448; J. Huth et al, *Proc. of the 1990 DPF Summer Study on High Energy Physics*, Snowmass, Colorado (1992) 134.
 29. M. Klasen, G. Kramer, *Phys. Rev.* **D56** (1997) 2702.
 30. ZEUS Coll., J. Breitweg et al., DESY-97-191 (hep-ex/9710002).
 31. G.Kramer, S.G.Salesch, *Phys. Lett.* **B333** (1994) 519; *Phys. Lett.* **B317** (1993) 218.
 32. S.D. Ellis, D.E. Soper, *Phys. Rev.* **D48** (1993) 3160.
 33. T. Kleinwort, G. Kramer, *Z. Phys.* **C75** (1997) 489; *Nucl. Phys.* **B477** (1996) 3; *Phys. Lett.* **B370** (1996) 141.
 34. P. Aurenche et al, *Progr. Theor. Phys.* **92** (1994) 175.
 35. P. Aurenche et al, *Proc. of "Future Physics at HERA"*, Hamburg (1996) 570; M. Klasen et al, *Z. Phys.* **C68** (1995) 1131; D. Bödeker et al, *Z. Phys.* **C63** (1994) 471; P. Aurenche et al, *Phys. Lett.* **B338** (1994) 98; L.E. Gordon, J.K. Storrow, *Phys. Lett.* **B291** (1992) 320; H. Baer et al, *Phys. Rev.* **D40** (1989) 2844.
 36. M. Klasen, G. Kramer, *Z. Phys.* **C76** (1997) 67; *Z. Phys.* **C72** (1996) 107.
 37. L.E. Gordon, J.K. Storrow, *Nucl. Phys.* **B489** (1997) 405;
 38. P. Aurenche, M. Fontannaz, J.P. Guillet, *Z. Phys.* **C64** (1994) 621.
 39. ZEUS Coll., paper 650 submitted to EPS'97, Jerusalem, August 1997.
 40. ZEUS Coll., paper 654 submitted to EPS'97, Jerusalem, August 1997.
 41. ZEUS Coll., paper 652 submitted to EPS'97, Jerusalem, August 1997.
 42. AMY Coll., B. J. Kim et al., *Phys. Lett.* **B325** (1994) 248.
 43. TOPAZ Coll., H. Hayashii et al., *Phys. Lett.* **B314** (1993) 149.
 44. OPAL Coll., K. Ackerstaff et al., *Z. Phys.* **C73** (1997) 433.

45. R. Engel, J. Ranft, *Phys. Rev.* **D54** (1996) 4244; R. Engel, *Z. Phys.* **C66** (1995) 203.
46. H. Abramowicz, K. Charchula, A. Levy, *Phys. Lett.* **B269** (1991) 458.
47. B.L. Combridge, C.J. Maxwell, *Nucl. Phys.* **B239** (1984) 429.
48. H1 Coll., C. Adloff et al., DESY-97-164 (hep-ex/9709004).
49. H1 Coll., paper 270 submitted to EPS'97, Jerusalem, August 1997.
50. H1 Coll., T. Ahmed et al., *Nucl. Phys.* **B445** (1995) 195.
51. PLUTO Coll., Ch. Berger et al., *Phys. Lett.* **B142** 119.
52. H1 Coll., C. Adloff et al., DESY-97-179 (hep-ex/9709017)
53. ZEUS Coll., paper 656 submitted to EPS'97, Jerusalem, August 1997.
54. L.E. Gordon, preprints hep-ph/9706355 and hep-ph/9707464.
55. M. Drees et al, *Phys. Lett.* **B306** (1993) 371.
56. M. Cacciari et al, *Nucl. Phys.* **B466** (1996) 173.
57. S. Frixione et al, *Phys. Lett.* **B348** (1995) 633; *Nucl. Phys.* **B454** (1995) 3.
58. B.A. Kniehl et al, DESY 96-210 (hep-ph/9610267); J. Binnewies et al, DESY 96-012 (hep-ph/9702408).
59. M. Cacciari, M. Greco, DESY 97-029 (hep-ph/9702389); M. Cacciari et al, *Phys. Rev.* **D55** (1997) 2736.
60. ALEPH Coll., *Phys. Lett.* **B355** (1995) 595.
61. L3 Coll., paper LP-092 submitted to this conference.
62. P. Aurenche et al., *Physics at LEP2*, CERN 96-01, p.328 (1996) and references therein.
63. H1 Coll., paper 276 submitted to EPS'97, Jerusalem, August 1997; H1 Coll., *Nucl. Phys.* **B472** (1996) 32.
64. ZEUS Coll., paper 276 submitted to EPS'97, Jerusalem, August 1997; ZEUS Coll., *Phys. Lett.* **B401** (1997) 192.
65. ZEUS Coll., *Phys. Lett.* **B349** (1995) 225.
66. E. Gallo, *Diffraction*, these proceedings and hep-ex/9710013.
67. M. Drees, R.M. Godbole, *Nucl. Phys.* **B339** (1990) 355; J.R. Forshaw, J.K. Storrow, *Phys. Rev.* **D46** (1992) 4955; M. Drees, R.M. Godbole, *Z. Phys.* **C59** (1993) 591; A. Corsetti et al., *proc. of PHOTON '97*, Egmond aan Zee, NL (1997).
68. PLUTO Coll., Ch. Berger et al., *Phys. Lett.* **B149** (1984) 421.
69. TPC/ 2γ Coll., H. Aihara et al., *Phys. Rev.* **D41** (1990) 2667.
70. S. E. Baru et al., *Z. Phys.* **C53** (1992) 219.
71. L3 Coll., M. Acciarri et al., *Phys. Lett.* **B408** 1997 450.
72. F. Wäckerle (OPAL Coll.), *proceedings of the XXVIII Int. Symposium on Multiparticle Dynamics*, Frascati, Italy (1997).
73. R. M. Barnett et al., *Review of Particle Physics*, *Phys. Rev.* **D54** (1996) 1.
74. G. A. Schuler, T. Sjöstrand, *Z. Phys.* **C73** (1997) 677.
75. L. Bourhis, M. Fontannaz, J.Ph. Guillet, hep-ph/9704447.
76. ALEPH Coll., D. Buskulic et al., *Z. Phys.* **C69** (1996) 365.
77. OPAL Coll., K. Akerstaff et al., CERN-PPE-97-86 (hep-ex/9708020).
78. J.F. Owens, *Rev. of Mod. Phys.* **59** (1987) 465; D.W. Duke, J.F. Owens, *Phys. Rev.* **D26** (1982) 1600.
79. M. Glück, E. Reya, A. Vogt, *Phys. Rev.* **D48** (1993) 116.